RSC Advances

PAPER

View Article Online
View Journal | View Issue

Cite this: *RSC Adv.*, 2019, **9**, 18803

Monometallic and bimetallic Cu–Ag MOF/MCM-41 composites: structural characterization and catalytic activity

W. S. Abo El-Yazeed * and Awad I. Ahmed

Received 3rd May 2019
Accepted 7th June 2019

DOI: 10.1039/c9ra03310f

rsc.li/rsc-advances

Monometallic and bimetallic MOF/MCM-41 composites (Cu, Ag and Cu–Ag) were synthesized *via* a solvothermal method. The synthesized composites were characterized by XRD, FTIR, SEM, EDX and BET surface area measurements. The acidity was determined through two techniques; potentiometric titration with *n*-butyl amine for determining the strength and the total number of acid sites and FTIR spectra of chemisorbed pyridine on the surface of MOFs for determining the type of acid sites (Brønsted and/or Lewis). All the prepared MOFs showed Lewis-acid sites and the higher acidity was observed for the bimetallic Cu–Ag MOF/MCM-41 composite. The catalytic activity was examined on the synthesis of 1-amidoalkyl-2-naphthol *via* the reaction of benzaldehyde, 2-naphthol and benzamide. The best yield (92.86%) was obtained in the least time (10 min) with a molar ratio 1.2 : 1.2 : 1.7 of benzaldehyde : β-naphthol : benzamide and 0.1 g bimetallic Cu–Ag MOF/MCM-41 composite under solvent-free conditions at 130 °C. Reuse of the catalysts showed that they could be used at least four times without any reduction in the catalytic activity.

1 Introduction

Nanoporous metal–organic frameworks (MOFs) have received more attention due to their attractive properties such as high surface area, high porosity, low density and crystalline character as well as their composition and chemical structure.[1–3] Therefore, MOFs used in various applications involving chemical separation,[4] gas adsorption and storage,[5] drug delivery,[6] luminescence,[7] biomedical imaging[8] and used in many reactions as a catalyst.[9] There is a strong host–guest interaction in the MOF between the metal nanoparticles and the framework *via* coordination and π–π forces which depend on its electronic properties and structure that in turn enhance the catalytic activity and stability.[10–12] MOF catalysts are nontoxic, inexpensive, have very high activity and selectivity, and can be separated easily from the reaction mixture and reused.[13] Nano MOFs often exhibit some additional chemical and physical properties, without changing the material composition, which differs from usual inorganic metal oxides.[14] Numerous methods have been used to control the shape and the size of MOF crystals, such as hydrothermal/solvothermal treatment,[15] ultrasonic synthesis,[16] microwave heating[17] and reverse microemulsion.[18] MOFs have been used as solid catalysts for some organic reactions as biodiesel production,[19] cyanosilylation of aldehydes,[20] synthesis of coumarins,[21] catalytic degradation of *o*/*m*/*p*-nitrophenol,[22] synthesis of indolizines through aldehyde–amine–alkyne couplings,[23] synthesis of 1,5-benzodiazepine,[24] Biginelli reaction,[25] oxidation,[26] aza-Michael condensation[27] and so on. However, due to the low thermal stability and processability of MOFs, the practical applications of them are limited.[28,29] Also, the dispersive forces for some MOFs are weak due to the high amount of void spaces.[30] To overcome these disadvantages, composites have been prepared by combining MOFs with other substrates[31,32] as graphene,[33] carbon nanotubes,[34] activated carbon,[35] metals[36] and silica.[37] Composites are considered as multicomponent materials which have special properties and many applications in the removal of pollutants and in the catalysis field.[38] Zhou *et al.* prepared a composite from three different MOFs and SBA-15 which enhanced the thermal stability of MOFs and increased the decomposition temperature from 318 to 350 °C.[39]

Hexagonal mesoporous MCM-41 materials has been discovered in 1992 as a member of the M41s family, family of siliceous materials, which possess some properties as large pore volume, large pore size (2–50 nm), controlled pore geometries, well-defined structure, uniform size distribution and high surface area (up to 1000 $m^2 g^{-1}$).[40] Therefore, MCM-41 materials applied in many fields as catalysts or catalyst supports.[41,42] The integration of MOFs on mesoporous materials as MCM-41 would produce multiple interfaces, which created synergistic effects from multiple components by integration of more than two active sites such as bimetallic or multimetallic catalysts which improve the catalytic activity.[43]

Amidoalkyl naphthol derivatives are one of the multicomponent reactions (MCRs) which have a great importance nowadays because of their essential role in organic synthesis as formation of desired products in a single synthetic process

Chemistry Department, Faculty of Science, Mansoura University, Mansoura, Egypt. E-mail: dr_ws2008@mans.edu.eg; Tel: +201008282160

without any separation problems which in role show high atom economy and high selectivity.[44] Amidoalkyl naphthol derivatives have many biological applications such as bradycardiac, antibacterial and hypotensive activities.[45,46]

Herein, we prepared composites of monometallic and bimetallic MOFs with MCM-41 to combine both properties of metal–organic frameworks and mesoporous materials in these composites.[3] Also, we studied their role in the formation of 1-amidoalkyl-2-naphthols.

2 Experimental

2.1. Materials

Terephthalic acid (H_2BDC) (98%) was purchased from ALPHA CHEMICA. Pure $Cu(NO_3)_2 \cdot 3H_2O$, $AgNO_3$, *N*,*N*-dimethylformamide (99.8%), tetra ethyl orthosilicate (TEOS), ammonium hydroxide (28%), benzamide, acetonitrile, *n*-butyl amine, pyridine, β-naphthol benzaldehyde and cethyltrimethylammonium-bromide (CTAB) were provided from Merck.

2.2. Catalyst preparation

2.2.1. Preparation of Cu-MOF/MCM-41 and Ag-MOF/MCM-41 composites. MCM-41 was prepared according to our previous literature.[47] Cu-MOF/MCM-41 and Ag-MOF/MCM-41 composites were achieved by the solvothermal method[48] as following: 0.4832 g (2 mmol) of $Cu(NO_3)_2 \cdot 3H_2O$ or 0.3397 g (2 mmol) of $AgNO_3$ and 0.3323 g (2 mmol) of terephthalic acid were dissolved in 40 ml of DMF solvent, then 10 ml distilled water containing 0.05 g MCM-41 was added and the mixture was stirred for 30 min. The two mixtures were transferred into two autoclaves and heated at 140 °C for 10 h. After cooling to room temperature, the precipitates were filtered and washed several times with DMF followed by drying under vacuum at 120 °C for 6 h. Finally, the blue powder of Cu-MOF/MCM-41 and gray powder of Ag-MOF/MCM-41 composites were obtained.

2.2.2. Preparation of bimetallic Cu–Ag MOF and Cu–Ag MOF/MCM-41 composite. In the same procedures, Cu–Ag MOF was prepared by mixing 0.2416 g (1 mmol) of $Cu(NO_3)_2 \cdot 3H_2O$, 0.1699 g (1 mmol) of $AgNO_3$ and 0.3323 g (2 mmol) of terephthalic acid and dissolved in 40 ml DMF solvent while Cu–Ag MOF/MCM-41 composite was prepared by mixing the same amounts with suspension of 0.05 g MCM-41.

2.3. Characterization techniques

FT-IR spectra were measured on the Thermo SCIENTIFIC (NICOLET iS10). The samples were mixed with dry KBr to be analyzed and then scanned from 400 to 4000 cm^{-1}. XRD patterns were collected on a PW 150 (Philips) using Ni-filtered Cu Kα radiation ($\lambda = 1.540$ Å) from 2θ of 4 to 80° at 40 kV. The morphology and the elements of the prepared samples were examined *via* SEM (Scanning Electron Microscopy) and EDX (Energy-Dispersive X-ray Spectroscopy) analysis with the JEOL (Model JSM-6510LV SEM) scanning electron microscope. Before the analysis the samples were coated with gold. To study the binding energies, X-ray photoelectron spectroscopic (XPS) was collected on K-alpha (Thermo Fisher Scientific, USA) with monochromatic X-ray Al K-alpha radiation (−10 to 1350 eV). The surface area of the prepared catalysts was determined by nitrogen adsorption measurement apparatus at −196 °C after degassing at 250 °C for 4 h under a pressure of 10^{-5} torr.

2.4. Acidity measurements

The total number of acid sites of the solid samples was determined by potentiometric titration.[49] 0.03 g of the solid catalyst activated at 120 °C for 2 h under vacuum was suspended in 20 ml acetonitrile under stirring for 3 h. The suspension was then titrated with (0.025 N) *n*-butyl amine in acetonitrile at 0.005 ml min^{-1}. The variation in the electrode potential after adding the *n*-butyl amine solution was measured with an Orion 420 digital A model using a double-junction electrode.

FTIR spectra of adsorbed pyridine were used to determine the Lewis and Brønsted acid sites on the surface of the examined catalysts.[50] Firstly, the samples were heated at 150 °C under vacuum for 2 h. liquid pyridine was added quickly to minimize the contact time with ambient atmosphere. The samples were maintained in contact with pyridine vapor, at room temperature, for 4 weeks, prior to analysis by FTIR. The excess pyridine was removed by drying the samples at 120 °C in an oven for 2 h. The FT-IR spectra of the pyridine-adsorbed on the samples were carried out using Thermo Scientific (Nicolet iS10) FTIR spectrophotometer by mixing 0.01 g of the sample with 0.1 g KBr in 30 mm diameter self-supporting discs.

2.5. Catalytic activity

For synthesis of 1-amidoalkyl-2-naphthol, a mixture of benzaldehyde (1.2 mmol), β-naphthol (1.2 mmol), benzamide (1.7 mmol) and 0.1 g of the MOF were mixed in a 100 ml round bottom flask and the subsequent mixture was stirred magnetically under solvent-free condition at 130 °C for the required time. After completion the reaction (confirmed by TLC), the reaction mixture was cooled to room temperature and washed several times with 10 ml hot water with continuous stirring to remove the unreacted starting materials. The product was filtered off and the separated catalyst was washed with ethanol and finally dried in an oven at 120 °C for reuse. Amidoalkyl-2-naphthol was collected from the filtrate and then recrystallized from ethanol.[45,51] The product was characterized by its melting point (235–237 °C) and FT-IR. The % yield of 1-amidoalkyl-2-naphthol can be calculated easily from the following equation:

$$\text{Yield (wt\%)} = \frac{\text{obtained weight of product}}{\text{thoretical weight of product}} \times 100$$

3 Results and discussion

3.1. X-ray diffraction analysis

The low and high-angle XRD patterns of pure MCM-41 were illustrated in Fig. 1a. At $2\theta = 2.4$, 4.0 and 4.6°, respectively, the

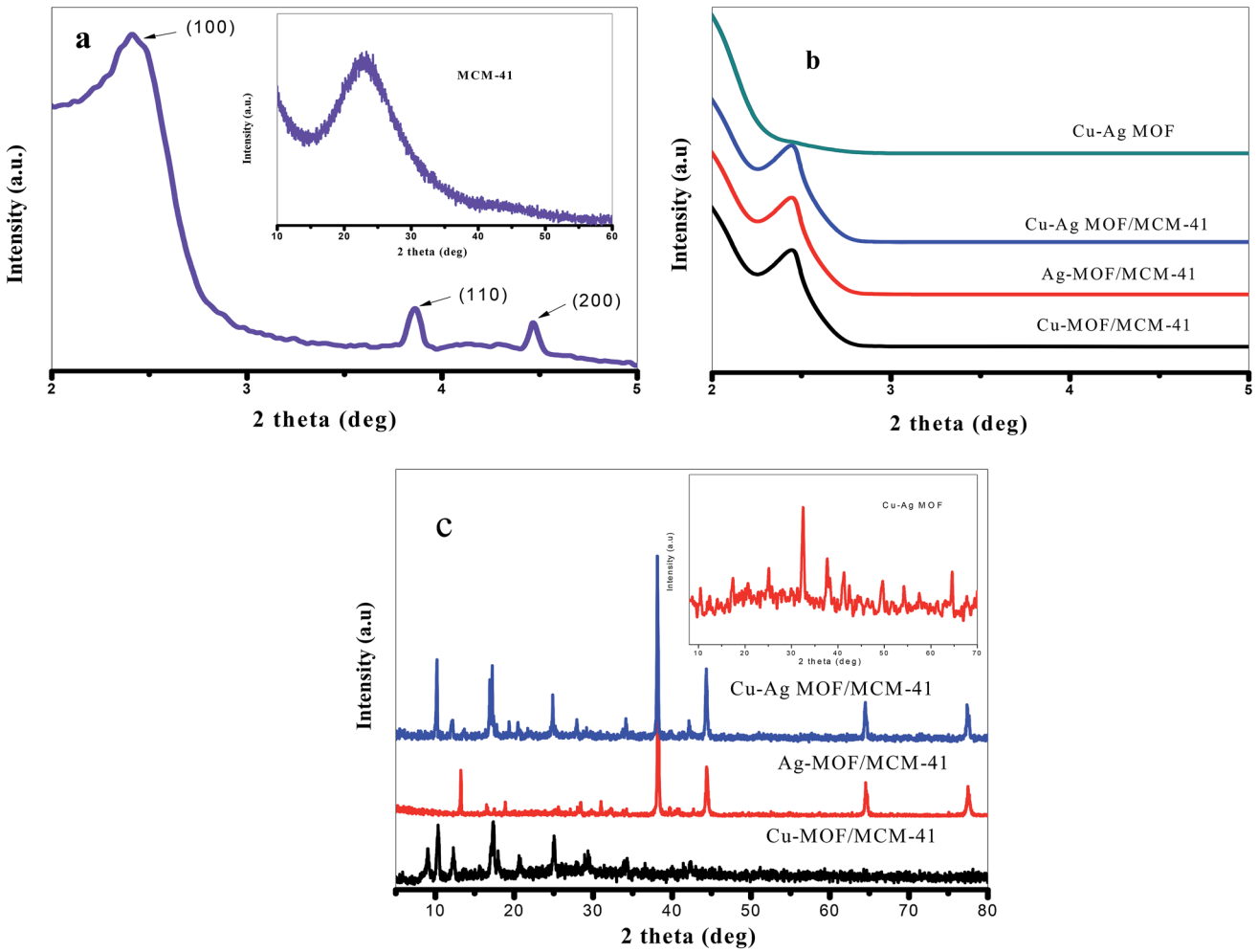

Fig. 1 (a) Low and high-angle XRD of MCM-41 and (b) low-angle and (c) high-angle XRD for the prepared catalysts.

three characteristic peaks of the ordered hexagonal mesoporous structure were observed, while at $2\theta = 10–60°$ there is abroad hump due to formation of an amorphous phase.[47] Fig. 1b shows that the MOF/MCM-41 composites still maintains the mesoporous structure of MCM-41 by the appearance of the peak (100) at 2.4°. The XRD patterns of Cu-MOF/MCM-41, Ag-MOF/MCM-41, Cu–Ag MOF/MCM-41 composites and Cu–Ag MOF are presented in Fig. 1c. All the main diffraction peaks of the octahedral Cu-MOF appeared in Cu-MOF/MCM-41 pattern at $2\theta =$ 9.03°, 10.23°, 12.34°, 17.36°, 20.67°, 24.92°, 29.30°, 34.33°, 42.12° which assigned to (220), (222), (400), (440), (442), (731), (751), (951) and (971), respectively. These peaks are in a good agreement with the patterns of Cu-MOF in the literature[52,53] indicating the successful preparation of the MOF. The peaks of Ag-MOF/MCM-41 composite appeared at $2\theta = 13.27°$, 16.74°, 18.93°, 28.51°, 30.88°, 38.11°, 44.37°, 64.46°, 77.35° in a good agreement with the literature.[54] The peaks at $2\theta = 38.11°$ (111), 44.37° (200), 64.46° (220) and 77.35° (311) corresponds to a face centered cubic of Ag species nanoparticles which may be produced from the reduction of Ag^+ to Ag metal with the aid of DMF as reducing agent.[55–58] The bimetallic Cu–Ag MOF/MCM-41 composite combines the characteristic peaks of both Cu-MOF and Ag-MOF with a small shift of the peaks of Cu to lower 2θ values supporting the successful preparation of bimetallic MOF.[59,60] Comparing the pattern of Cu–Ag MOF with that of Cu–Ag MOF/MCM-41, the intensities of the main diffraction peaks of Cu and Ag-MOF are decreased meaning that MCM-41 enhances the crystallinity of the MOF/MCM-41 composites.

3.2. FT-IR spectroscopy

The FT-IR spectra of the prepared MOFs are shown in Fig. 2. The spectra of pure MCM-41, Cu-MOF/MCM-41, Ag-MOF/MCM-41, Cu–Ag-MOF/MCM-41 and Cu–Ag MOF exhibit clear absorption spectra corresponding to metal–organic framework structure with a little shift in the wavelengths. The FT-IR spectra in the region 700–1200 cm^{-1} attributed to the fingerprint of terephthalate compounds in which the absorption over 900 cm^{-1} is related to the bending aromatic C–H (in plane) and the absorption lower than 900 cm^{-1} is related to the bending aromatic C–H (out plane) of terephthalic acid linker.[55,61,62] The stretching band of C–H groups related to linker is appeared at 2999 cm^{-1}[63] Also, the peaks at 1621 and 1393 cm^{-1} are related

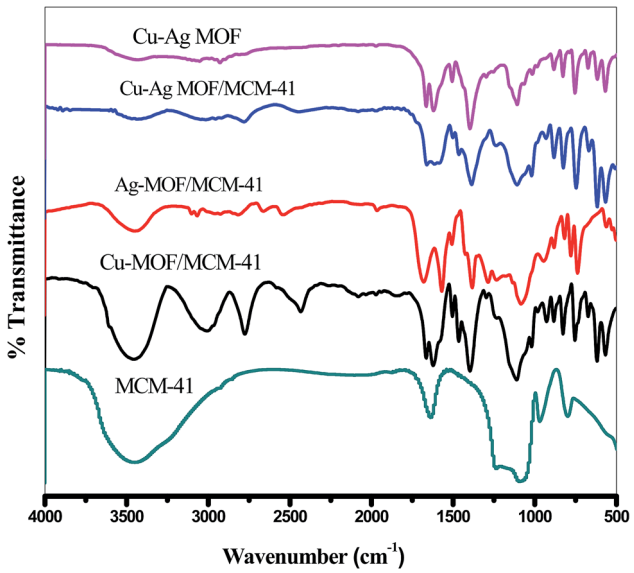

Fig. 2 FTIR spectra of the prepared catalysts.

to the carboxylate ligands. The vibration absorption spectra of the C–O group of free carboxylic acids are observed at 1666 and 1470 cm^{-1}[164] and the peaks at 575, 621 and 674 cm^{-1} belongs to the stretching vibrations of the Cu–O.[65,66] Also, the broad band appeared at 3456 cm^{-1} in the FT-IR spectra of Cu-MOF/MCM-41 and Ag-MOF/MCM-41 composites attributes to the vibration of coordinated water molecules.[67] MOF/MCM-41 composites exhibit bands of MCM-41 at 803, 959 and 1252 cm^{-1} with a little shift which is good evidence on maintaining the mesoporous structure of MCM-41.[47,68] The disappearance of the broad spectra at 3456 cm^{-1} in the FT-IR spectra of Cu–Ag MOF/MCM-41 composite and Cu–Ag MOF indicates the removal of the water during the formation of bimetallic MOF.

3.3. SEM and EDX

The SEM and EDX images of Cu-MOF/MCM-41, Ag-MOF/MCM-41, Cu–Ag MOF/MCM-41 composites and Cu–Ag MOF are presented in Fig. 3. The SEM image of Fig. 3a displays the dispersion of octahedral Cu structure on the surface of MCM-41,[64,69] while Fig. 3b shows the dispersed irregular spherical Ag particles with different sizes the surface of MCM-41.[70] There is a significant difference in the surface morphology of the two bimetallic MOFs, Cu–Ag MOF/MCM-41 composite and Cu–Ag MOF (Fig. 3(c and d), respectively). The images show that the agglomeration of irregular small Ag particles increased after the addition of MCM-41 which resulted in the appearance of more dispersed blocks on its surface. This explains the significant effect of the incorporation of MCM-41 during the formation of MOF and the high dispersion of the Cu–Ag MOF inside and outside the pores of MCM-41.[66,68,71] The EDX spectra in Fig. 3(e and f) reveal the contribution of C, O, Cu, Ag, and Si elements in the Cu–Ag MOF/MCM-41 composite structure while C, O, Cu and Ag elements in the Cu–Ag MOF structure.

3.4. X-ray photoelectron spectroscopic (XPS)

To determine the chemical composition of Cu–Ag MOF/MCM-41 composite and the chemical state of its elements, XPS was performed (Fig. 4.). As shown in the XPS survey scan (Fig. 4a.), the Cu–Ag MOF/MCM-41 composite contains Cu, Ag, C, O and Si elements which consisted with the EDX results. The C 1s XPS spectrum (Fig. 4b.) reveals three peaks at 284.79, 286.35 and 288.62 eV which are attributed to C–C & C–H & C=C, C–O and O–C–O groups, respectively.[72] O 1s emission spectrum (Fig. 4c.) has two main peaks at 531.72 eV (characteristic of metal–oxygen bonds) and 533.17 eV (characteristic of the O–H groups).[73] The Si 2p emission spectrum shows only one peak at 103.52 eV

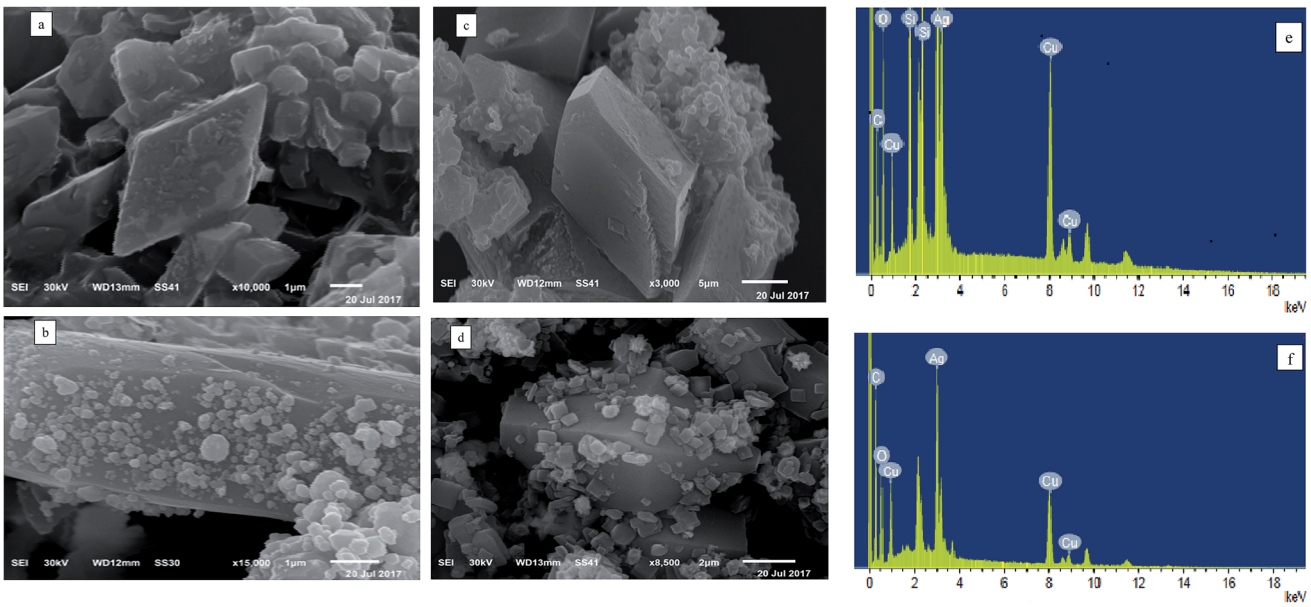

Fig. 3 SEM images of ((a) Cu-MOF/MCM-41, (b) Ag-MOF/MCM-41, (c) Cu–Ag MOF/MCM-41 and (d) Cu–Ag MOF) and EDX analysis of ((e) Cu-MOF/MCM-41 and (f) Cu–Ag MOF).

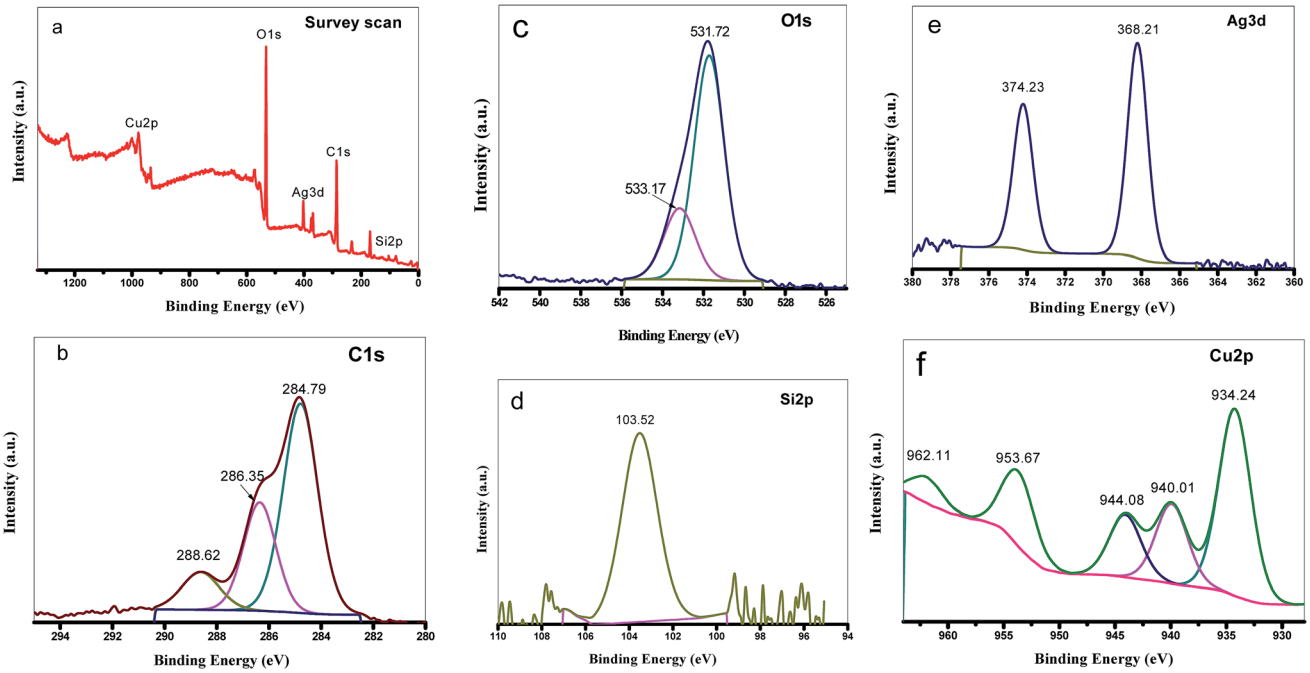

Fig. 4 XPS spectra of Cu–Ag MOF/MCM-41 composite: (a) the survey scan, (b) C 1s, (c) O 1s, (d) Si 2p, (e) Ag 3d and (f) Cu 2p.

(Fig. 4d.). Ag 3d XPS spectrum (Fig. 4e.) exhibits two main peaks at 368.21 eV (Ag $3d_{3/2}$) and 374.23 eV (Ag $3d_{5/2}$) which are ascribed to metallic Ag. The 6 eV spin-energy separation between the two peaks of Ag 3d confirmed on the presence of Ag^0 in the Cu–Ag MOF/MCM-41 composite[54,74] that may be produced from the reduction of Ag^+ to Ag metal with the aid of DMF as reducing agent as explained in XRD results. The high resolution spectrum of Cu 2p exhibits five peaks at 934.24, 940.01, 944.08, 953.67 and 962.11 eV (Fig. 4f.). The peaks at 934.24 and 953.67 eV were assigned to Cu 2p3/2 and Cu $2p_{1/2}$ of Cu–O. The presence of overlapping satellite peaks at 940.01 and 944.08 eV for Cu $2p_{3/2}$ and at 962.11 eV for Cu $2p_{1/2}$ indicated the presence of CuO (Cu^{2+}) or Cu_2O (Cu^{1+}) species in the composite.[75,76]

3.5. Surface area measurements

The porosity of the prepared materials was characterized by N_2 adsorption–desorption isotherms at −196 °C. As shown in Fig. 5a., the Cu, Ag and Cu–Ag MOF/MCM-41 composites exhibit type IV isotherm typical of mesoporous materials with H_3 hysteresis loop. A linear increase in N_2 adsorption at low relative pressure is observed due to the formation of monolayer followed by the capillary condensation of N_2 inside the mesopores.[63] The Cu–Ag MOF exhibits type I isotherm indicating the microporous nature of the MOF with H_3 hysteresis loop indicating the presence of cylindrical pores.[71] The derived porosity parameters, surface area and pore volume, were calculated and listed in Table 1. The surface area of MCM-41 was 1389.2 $m^2\ g^{-1}$ as mentioned previously in our literature,[47] while the pore volume was 3.63 $cm^3\ g^{-1}$. Ag-MOF/MCM-41, Cu-MOF/MCM-41 and Cu–Ag MOF/MCM-41 composites have a BET surface area 296.4, 545.2 and 594.8 $m^2\ g^{-1}$, respectively which are lower than that of MCM-41. This can be explained by the partial blocking of the pores of MCM-41 through the dispersion of the MOF particles inside and/or outside them although the maintaining of the mesostructure which is very important for catalysis applications.[77,78] This was confirmed also by the decrease in the pore volume. The increase in the surface area and pore volume of the bimetallic Cu–Ag MOF compared with each monometallic MOF is observed that may be resulted from the creation of new micropores arises from two metals Cu and Ag in the bimetallic MOF. These values increases when the bimetallic MOF composited with MCM-41 as a result of presence of both meso and micropores. The pore size distribution curves (Fig. 5b.) for all samples exhibit a narrow micropores peak characteristic of the MOF centered at 1.27 nm. The MOF/MCM-41 composites show also a mesoporous nature with two maxima from 10 to 50 nm. Cu-MOF/MCM-41 and Cu–Ag MOF/MCM-41 composites reveals two peak centered at 14 and 33 nm while Ag-MOF/MCM-41 composite reveal two peaks centered at 14 and 25 nm.

3.6. Surface acidity

3.6.1. Nonaqueous potentiometric titration. To determine the strength and the total number of acid sites on the MOFs surface, we used the potentiometric titration for the prepared MOFs with *n*-butyl amine[79] and the curves are shown in Fig. 6. The acid strength of these sites can be determined from the value of the initial electrode potential (E_i) and classified as follows: (i) when E_i is increased than 100 mV, the sites are classified as very strong acid sites,(ii) when E_i is between 0 and 100 mV, the sites are strong sites, (iii) when E_i is between −100 and 0 mV, the sites are weak sites, and (iv) when E_i is less than −100 mV, the sites are very weak sites.[80] From Fig. 6 and Table 1,

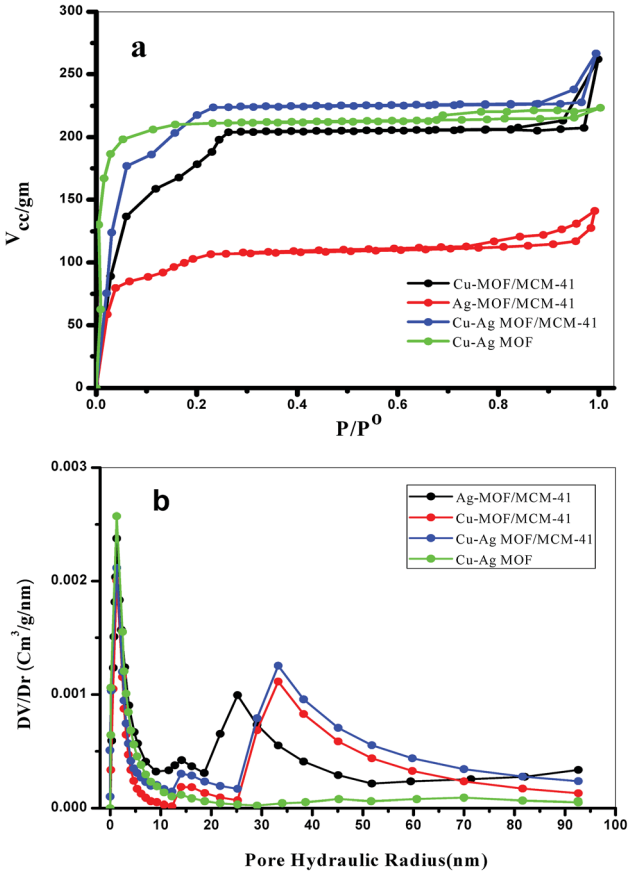

Fig. 5 (a) N_2 adsorption–desorption isotherms and (b) pore size distribution of the prepared composites.

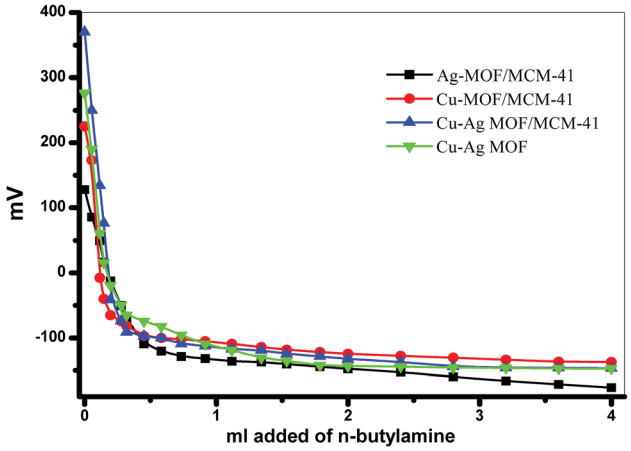

Fig. 6 Potentiometric titration curves of *n*-butyl amine in acetonitrile for the prepared catalysts.

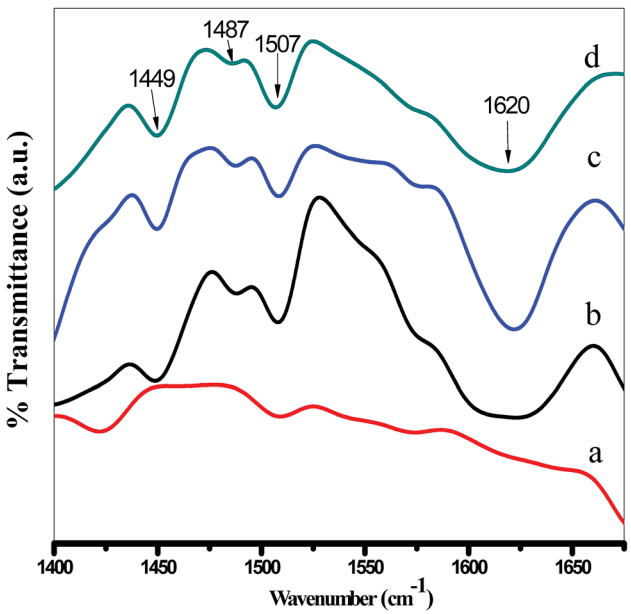

Fig. 7 FTIR spectra of adsorbed pyridine on (a) Ag-MOF/MCM-41, (b) Cu-MOF/MCM-41, (c) Cu–Ag MOF/MCM-41 and (d) Cu–Ag MOF.

the values of the initial electrode potential indicate that all the prepared MOFs have very strong acid sites and Cu–Ag MOF/MCM-41 composite has the highest number of total acid sites and the highest E_i value.

3.6.2. FTIR spectra of chemisorbed pyridine. The infrared spectra of adsorbed pyridine on the surface of the MOFs were used to determine the type of acid sites whether Brønsted or Lewis as shown in Fig. 7. The spectra show two bands at 1507 and 1421 cm^{-1} on Ag-MOF/MCM-41 composite and four bands in the samples Cu-MOF/MCM-41, Cu–Ag MOF/MCM-41 composites and Cu–Ag MOF at 1449, 1487, 1507 and 1620 cm^{-1} which are assigned to the adsorbed pyridine on Lewis acidic sites.[81–83]

3.7. Catalytic activity (synthesis of 1-amidoalkyl-2-naphthol)

The catalytic activity was examined by synthesis of pharmaceutically important 1-amidoalkyl-2-naphthol. Firstly, to optimize various reaction parameters, we performed some trials for the synthesis of 1-amidoalkyl-2-naphthol as a model reaction on MOF catalyst; the conditions of a MOF amount and the reactants molar ratio under solvent free condition at 130 °C are examined.

3.7.1. Effect of the MOF amount. The effect of Cu–Ag MOF/MCM-41 composite amount on the synthesis of 1-amidoalkyl-2-

Table 1 Surface and acidic properties of the prepared catalysts

Catalyst	S_{BET} (m^2 g^{-1})	V_t (cm^3 g^{-1})	E_i (mV)	No. of acid sites/g × 10^{-20}
Cu-MOF/MCM-41	545.2	0.32	225.1	1.64
Ag-MOF/MCM-41	296.4	0.18	128.2	1.34
Cu–Ag MOF/MCM-41	594.8	0.37	369.9	2.46
Cu–Ag MOF	551.3	0.34	276.2	2.03

Table 2 Synthesis of 1-amidoalkyl-2-naphthol under solvent free conditions at 130 °C

Catalyst	Catalyst weight (g)	Molar ratio benzaldehyde : β-naphthol : benzamide	Time (min)	Yield (%)	Apparent rate (min^{-1})
Cu-MOF/MCM-41	0.1	1.2 : 1.2 : 1.7	20	80.2	0.401
Ag-MOF/MCM-41	0.1	1.2 : 1.2 : 1.7	25	65.1	0.260
Cu–Ag MOF/MCM-41	0.1	1.2 : 1.2 : 1.7	10	92.86	0.929
Cu–Ag MOF	0.1	1.2 : 1.2 : 1.7	12	87.38	0.728
Cu–Ag MOF/MCM-41	0.1	1.2 : 1.2 : 1.2	60	40.23	0.067
Cu–Ag MOF/MCM-41	0.1	1.2 : 1.2 : 1.5	20	87.62	0.438
Cu–Ag MOF/MCM-41	0.1	1.2 : 1.2 : 1.9	30	79.52	0.265
Cu–Ag MOF/MCM-41	0.03	1.2 : 1.2 : 1.7	60	60.97	0.339
Cu–Ag MOF/MCM-41	0.05	1.2 : 1.2 : 1.7	25	80.95	0.648
Cu–Ag MOF/MCM-41	0.08	1.2 : 1.2 : 1.7	13	90.48	0.870
Cu–Ag MOF/MCM-41	0.13	1.2 : 1.2 : 1.7	10	92.91	0.715

naphthol was planned using 1.2 : 1.2 : 1.7 benzaldehyde : β-naphthol : benzamide under solvent free condition at 130 °C. Initially, the reaction was carried out without MOF catalyst under similar condition, but no yield was formed even after 12 h. Increasing the amount of MOF from 0.03 to 0.1 g led to increase the yield of 1-amidoalkyl-2-naphthol from 60.97% to 92.86% and the time was decreased from 60 min to 10 min indicating that 0.1 g of the catalyst was the best percentage of the yield after 10 min. On increasing the amount of the catalyst to 0.13 g, there is no improvement of the yield of 1-amidoalkyl-2-naphthol as illustrated in Table 2 and Fig. 8.

3.7.2. Effect of the molar ratio of the reactants. The reaction was performed on 0.1 g Cu–Ag MOF/MCM-41 composite under solvent free condition at 130 °C by using different molar ratio of the reactants. The best yield was obtained with a molar ratio 1.2 : 1.2 : 1.7 of benzaldehyde : β-naphthol : benzamide after 10 min as shown in Table 2 and Fig. 9.

3.7.3. Effect of MOF type. The synthesis of 1-amidoalkyl-2-naphthol reaction was carried out using 0.1 g of different MOFs (Cu-MOF/MCM-41, Ag-MOF/MCM-41, Cu–Ag MOF/MCM-41 composites and Cu–Ag MOF) using 1.2 : 1.2 : 1.7 benzaldehyde : β-naphthol : benzamide molar ratio under solvent free condition at 130 °C. The catalytic activity of the prepared bimetallic catalysts is increased compared with that of the monometallic catalyst which could be attributed to the presence of two different metals Cu and Ag and/or changing the active sites dispersion on the MOF surface in the bimetallic catalyst.[5,12,84–86] The results in Fig. 10 and Table 2 illustrate that Cu–Ag MOF/MCM-41 composite is the best catalyst with respect to reaction times (10 min) and yields (92.86%) of the products. The enhancement in the catalytic activity of this composite may be due to the following four factors: (i) the various active sites on the MOF surface with higher strength and acidity especially Lewis acid sites, (ii) the high surface area (iii) the presence of both meso and micropores and (iv) the presence of both Cu and Ag metals.

In comparison with other literatures; 1-amido alkyl-2-naphthol was obtained under solvent free conditions with a yield of 88% after 20 min using graphene oxide as a catalyst at 120 °C, 86% after 75 min using $Ba_3(PO_4)_2$ catalyst at 100 °C and 90% after 25 min using sulfonated poly-naphthalene at 80 °C.[45,87,88]

A possible mechanism for the synthesis of 1-amidoalkyl-2-naphthol was suggested in Scheme 1, based on the literature.[89] The reaction of benzaldehyde with β-naphthol in the

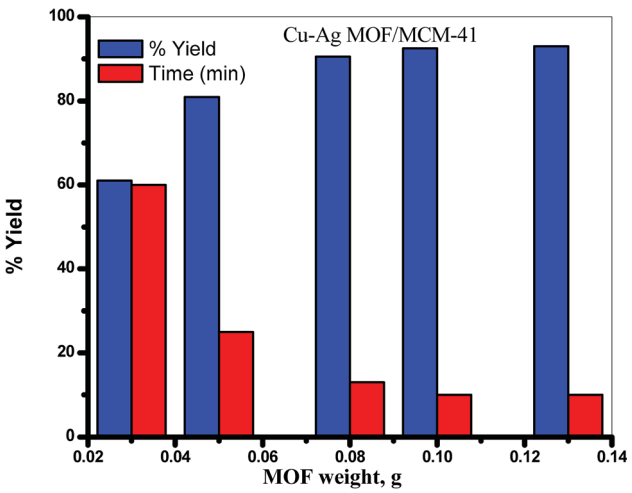

Fig. 8 Effect of the MOF weight on the synthesis of 1-amidoalkyl-2-naphthol.

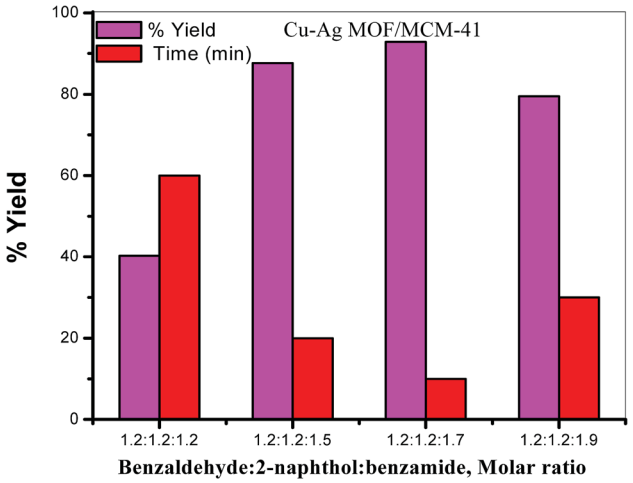

Fig. 9 Effect of the molar ratio of reactants on the synthesis of 1-amidoalkyl-2-naphthol.

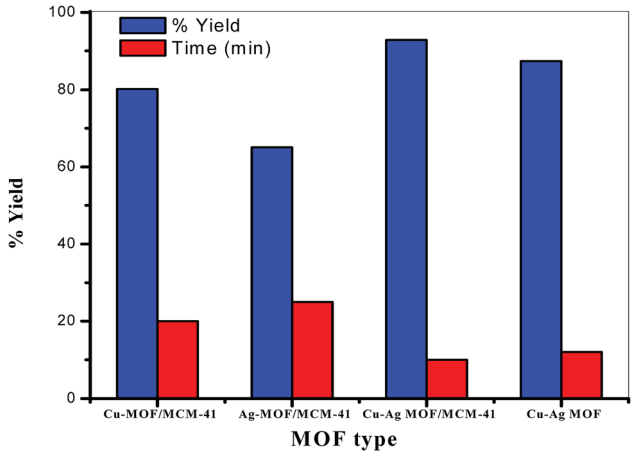

Fig. 10 Effect of the MOF type on the synthesis of 1-amidoalkyl-2-naphthol.

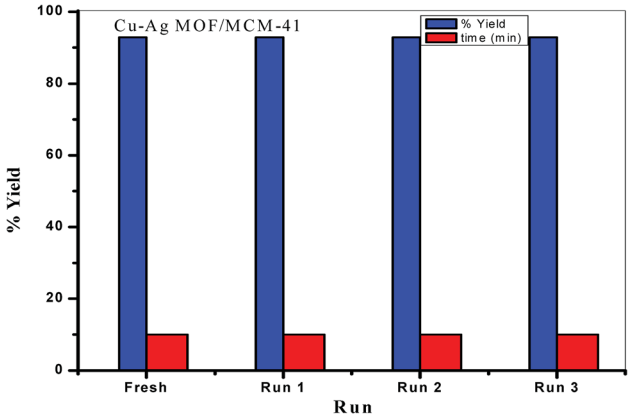

Fig. 11 Reuse of the Cu–Ag MOF/MCM-41 composite.

presence of MOF catalyst produces *ortho*-quinone methides (*o*-QMs) which reacted with benzamide *via* conjugated addition on the α,β-unsaturated carbonyl group to yield 1-amidoalkyl-2-naphthol. It was found that using benzaldehyde as aromatic aldehyde is better than aliphatic aldehyde which gave low yield in previous reports,[90,91] this can be attributed to an *o*-QMs intermediate produced from aliphatic aldehydes is less stable than that with aromatic aldehyde.

3.7.4. Reusability of the catalyst. The reusability is one of the most important characteristics of any catalyst. The recycling experiment was carried out with benzaldehyde, β-naphthol and benzamide under the same conditions as described above for the Cu–Ag MOF/MCM-41 composite catalyst. To maintain constant catalyst weight (0.1 g) during reusability experiments, we performed each experiment four times using the Cu–Ag MOF/MCM-41 composite in the same time and the second, third and fourth recycles are carried out by the same catalyst and constant weights. We found that Cu–Ag MOF/MCM-41 composite can be used four times without

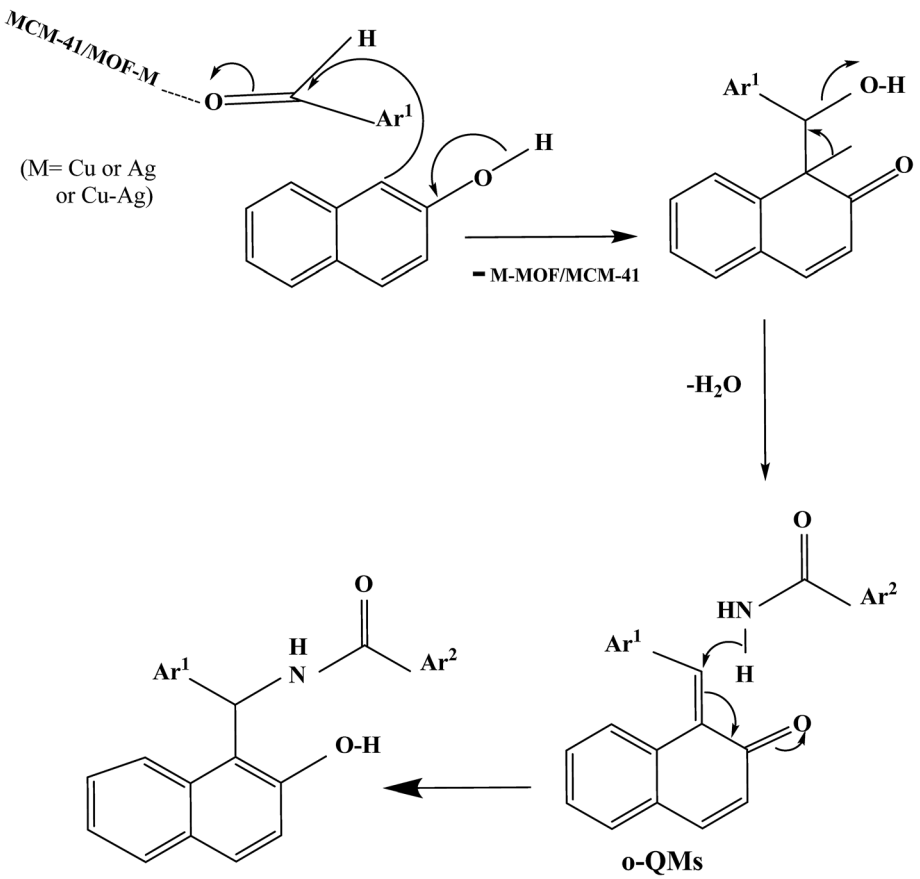

Scheme 1 A possible mechanism for the synthesis of 1-amidoalkyl-2-naphthol.

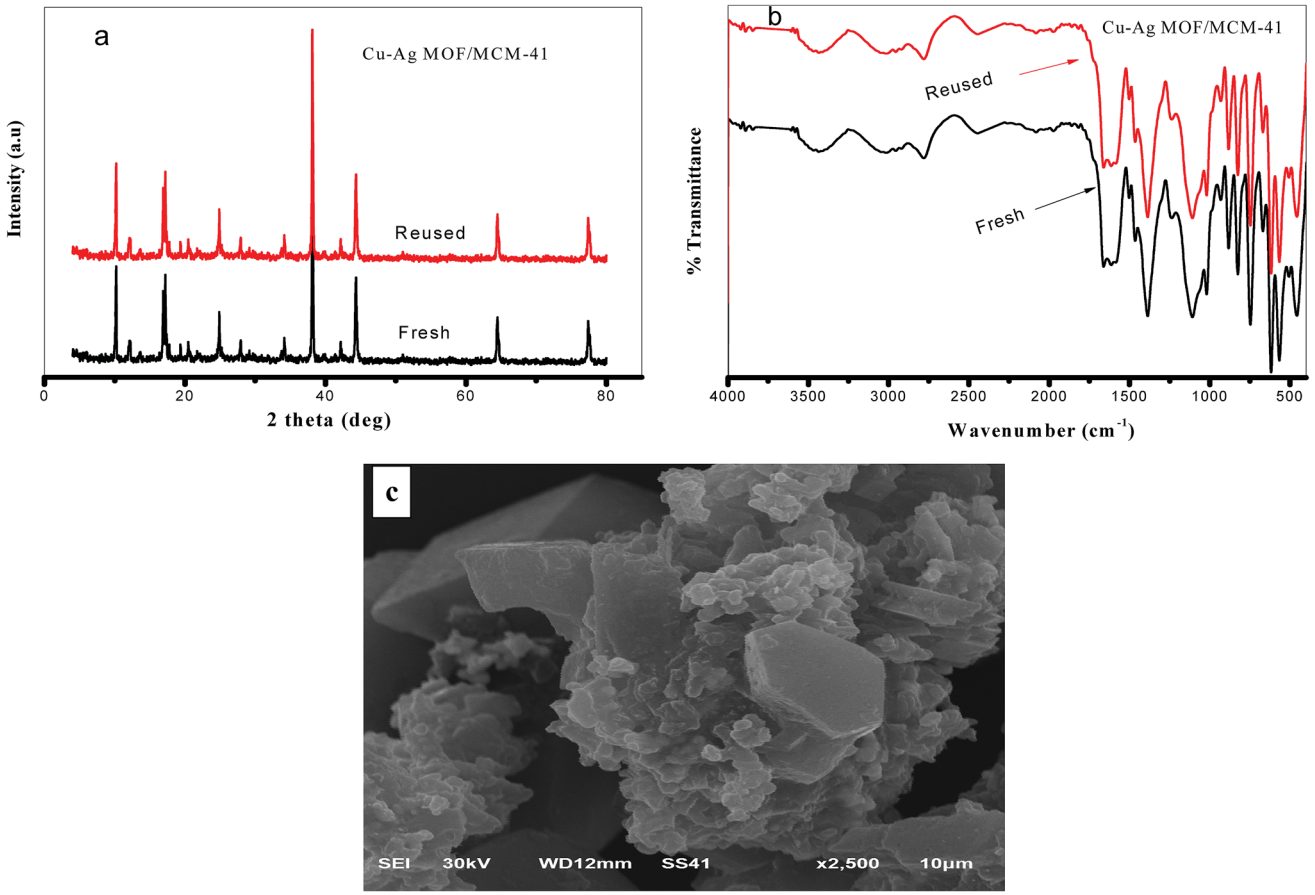

Fig. 12 (a) XRD, (b) FTIR and (c) SEM analysis of reused Cu–Ag MOF/MCM-41 composite after catalytic reaction.

any reduction in the catalytic activity (Fig. 11.). The FTIR, XRD and SEM analysis were determined for the fresh and reused Cu–Ag MOF/MCM-41 composite as shown in Fig. 12.

4 Conclusion

We found that MCM-41 enhanced the crystallinity and the catalytic activity of the prepared MOFs. The bimetallic Cu–Ag MOF/MCM-41 composite in comparing with other MOFs has the highest Lewis acidity and gave the best yield (92.86%) of 1-amidoalkyl-2-naphthol in 10 min. The enhancement in the catalytic activity of this bimetallic MOF/MCM-41 composite could be attributed to its well acidity, its high surface area, the presence of both meso and micropores and the presence of both Cu and Ag metals.

Conflicts of interest

There are no conflicts to declare.

References

1 J. Zhao, Y. Wang, J. Zhou, P. Qi, S. Li, K. Zhang, X. Feng, B. Wang and C. Hu, *J. Mater. Chem. A*, 2016, **4**, 7174–7177.
2 S.-J. Lee, K. C. Kim, T.-U. Yoon, M.-B. Kim and Y.-S. Bae, *Microporous Mesoporous Mater.*, 2016, **236**, 284–291.
3 Q.-L. Zhu and Q. Xu, *Chem. Soc. Rev.*, 2014, **43**, 5468–5512.
4 J.-R. Li, R. J. Kuppler and H.-C. Zhou, *Chem. Soc. Rev.*, 2009, **38**, 1477–1504.
5 X. Yang and Q. Xu, *Cryst. Growth Des.*, 2017, **17**(4), 1450–1455.
6 J. An, S. J. Geib and N. L. Rosi, *J. Am. Chem. Soc.*, 2009, **131**, 8376–8377.
7 M. D. Allendorf, C. A. Bauer, R. K. Bhakta and R. J. Houk, *Chem. Soc. Rev.*, 2009, **38**, 1330–1352.
8 X. Lian and B. Yan, *RSC Adv.*, 2016, **6**, 11570–11576.
9 J. Xiao, Y. Wu, M. Li, B. Y. Liu, X. C. Huang and D. Li, *Chem.–Eur. J.*, 2013, **19**, 1891–1895.
10 Q. Yuan, D. Zhang, L. V. Haandel, F. Ye, T. Xue, E. J. M Hensen and Y. Guan, *J. Mol. Catal. A: Chem.*, 2015, **406**, 58–64.
11 D. Zhang, Y. Guan, E. J. M. Hensen, T. Xue and Y. Wang, *Catal. Sci. Technol.*, 2014, **4**, 795–802.
12 B. Xia, C. Liu, H. Wu, W. Luo and G. Cheng, *Int. J. Hydrogen Energy*, 2015, **40**, 16391–16397.
13 P. Puthiaraj, A. Ramu and K. Pitchumani, *Asian J. Org. Chem.*, 2014, **3**, 784–791.
14 M. Y. Masoomi and A. Morsali, *RSC Adv.*, 2013, **3**, 19191–19218.
15 X. Cheng, A. Zhang, K. Hou, M. Liu, Y. Wang, C. Song, G. Zhang and X. Guo, *Dalton Trans.*, 2013, **42**, 13698–13705.

16 Z.-Q. Li, L.-G. Qiu, T. Xu, Y. Wu, W. Wang, Z.-Y. Wu and X. Jiang, *Mater. Lett.*, 2009, **63**, 78–80.
17 J. Klinowski, F. A. A. Paz, P. Silva and J. Rocha, *Dalton Trans.*, 2011, **40**, 321–330.
18 W. J. Rieter, K. M. L. Taylor, H. An, W. Lin and W. Lin, *J. Am. Chem. Soc.*, 2006, **128**, 9024–9025.
19 A. Nikseresht, A. Daniyali, M. A. Mohammadi, A. Afzalinia and A. Mirzaie, *Ultrason. Sonochem.*, 2017, **37**, 203–207.
20 I.-H. Choi, Y. Kim, D. N. Lee and S. Huh, *Polyhedron*, 2016, **105**, 96–103.
21 T. N. Lieu, K. D. Nguyen, D. T. Le, T. Truong and N. T. S. Phan, *Catal. Sci. Technol.*, 2016, **6**, 5916–5926.
22 X.-Q. Wu, G.-X. Wen, Y.-P. Wu, W.-W. Dong, J. Zhao and D.-S. Li, *J. Solid State Chem.*, 2016, **42**, 243–247.
23 G. H. Dang, H. Q. Lam, A. T. Nguyen, D. T. Le, T. Truong and N. T. S. Phan, *J. Catal.*, 2016, **337**, 167–176.
24 T. D. Le, K. D. Nguyen, V. T. Nguyen, T. Truong and N. T. S. Phan, *J. Catal.*, 2016, **333**, 94–101.
25 P. Li, S. Regati, R. J. Butcher, H. D. Arman, Z. Chen, S. Xiang, B. Chen and C.-G. Zhao, *Tetrahedron Lett.*, 2011, **52**, 6220–6222.
26 G. Chen, S. Wu, H. Liu, H. Jiang and Y. Li, *Green Chem.*, 2013, **15**, 230–235.
27 L. T. L. Nguyen, T. T. Nguyen, K. D. Nguyen and N. T. S. Phan, *Appl. Catal., A*, 2012, **425/426**, 44–52.
28 M. Ghorbanloo, V. Safarifard and A. Morsali, *New J. Chem.*, 2017, **41**, 3957–3965.
29 S. Li and F. Huo, *Nanoscale*, 2015, **7**, 7482–7501.
30 L. Li, X. L. Liu, H. Y. Geng, B. Hu, G. W. Song and Z. S. Xu, *J. Mater. Chem. A*, 2013, **1**, 10292–10299.
31 T. Han, Y. Xiao, M. Tong, H. Huang, D. Liu, L. Wang and C. Zhong, *Chem. Eng. J.*, 2015, **275**, 134–141.
32 T. Wehner, K. Mandel, M. Schneider, G. Sextl and K. Müller-Buschbaum, *ACS Appl. Mater. Interfaces*, 2016, **8**, 5445–5452.
33 B. Szczęśniak, J. Choma and M. Jaroniec, *Microporous Mesoporous Mater.*, 2019, **279**, 387–394.
34 F. Wang, X. Chen, L. Chen, J. Yang and Q. Wang, *Mater. Sci. Eng., C*, 2019, **96**, 41–50.
35 Y. Liu, P. Ghimire and M. Jaroniec, *J. Colloid Interface Sci.*, 2019, **535**, 122–132.
36 Y. Han, H. Xu, Y. Su, Z.-l. Xu, K. Wang and W. Wang, *J. Catal.*, 2019, **370**, 70–78.
37 R. Ameloot, A. Liekens, L. Alaerts, M. Maes, A. Galarneau, B. Coq, G. Desmet, B. F. Sels, J. F. M. Denayer and D. E. De Vos, *Eur. J. Inorg. Chem.*, 2010, **24**, 3735–3738.
38 M. Florent and T. Bendosz, *Microporous Mesoporous Mater.*, 2015, **204**, 8–14.
39 L. B. Sun, J. R. Li, W. Lu, Z. Y. Gu, Z. Luo and H. C. Zhou, *J. Am. Chem. Soc.*, 2012, **134**(38), 15923–15928.
40 S. K. Sharma, K. Sudarshan, D. Sen and P. K. Pujari, *J. Solid State Chem.*, 2019, **279**, 10–17.
41 N. Cakiryilmaz, H. Arbag, N. Oktar, G. Dogu and T. Dogu, *Catal. Today*, 2019, **323**, 191–199.
42 Y. Chi, J. Xue, J. Zhuo, D. Zhang, M. Liu and Q. Yao, *Sci. Total Environ.*, 2018, **633**, 1105–1113.
43 G. Zhan and H. C. Zeng, *Coord. Chem. Rev.*, 2016, **320–321**, 181–192.
44 A. Chinnappan, A. H. Jadhav, W.-J. Chung and H. Kim, *J. Mol. Liq.*, 2015, **212**, 413–417.
45 S. A. Pourmousavi, P. Moghimi, F. Ghorbani and M. Zamani, *J. Mol. Struct.*, 2017, **1144**, 87–102.
46 M. N-Esfahani, M. Montazerozohori and M. Taei, *C. R. Chim.*, 2016, **19**, 986–994.
47 A. I. Ahmed, S. E. Samra, S. A. El-Hakam, A. S. Khder, H. Z. El-Shenawy and W. S. Abo El-Yazeed, *Appl. Surf. Sci.*, 2013, **282**, 217–225.
48 T. Han, C. Li, X. Guo, H. Huang, D. Liu and C. Zhong, *Appl. Surf. Sci.*, 2016, **390**, 506–512.
49 A. I. Ahmed, S. A. El-Hakam, A. S. Khder and W. S. Abo El-Yazeed, *J. Mol. Catal. A: Chem.*, 2013, **366**, 99–108.
50 A. I. Ahmed, S. A. El-Hakam, M. A. Abd Elghany and W. S. Abo El-Yazeed, *Appl. Catal., A*, 2011, **407**, 40–48.
51 A. Davoodnia, R. Mahjoobin and N. Tavakoli-Hoseini, *Chin. J. Catal.*, 2014, **35**, 490–495.
52 S. Rostamnia, H. Alamgholiloo and X. Liu, *J. Colloid Interface Sci.*, 2016, **469**, 310–317.
53 A. R. Abbasi, M. Karimi and K. Daasbjerg, *Ultrason. Sonochem.*, 2017, **37**, 182–191.
54 H. Guo, Y. Zhang, Z. Zheng, H. Lin and Y. Zhang, *Talanta*, 2017, **170**, 146–151.
55 D. K. Yadav, V. Ganesan, F. Marken, R. Gupta and P. K. Sonkar, *Electrochim. Acta*, 2016, **219**, 482–491.
56 R. Gupta and V. Ganesan, *Sens. Actuators, B*, 2015, **219**, 139–145.
57 P. K. Sonkar and V. Ganesan, *J. Solid State Electrochem.*, 2015, **19**, 2107–2115.
58 P. K. Rastogi, V. Ganesan and S. A. Krishnamoorthi, *J. Mater. Chem. A*, 2013, **2**, 933–943.
59 J. Yang, C. Zheng, P. Xiong, Y. Li and M. Wei, *J. Mater. Chem. A*, 2014, **2**, 19005–19010.
60 Z. Zhou, L. Mei, C. Ma, F. Xu, J. Xiao, Q. Xia and Z. Li, *Chem. Eng. Sci.*, 2016, **147**, 109–117.
61 S. R. Thakare and S. M. Ramteke, *Catal. Commun.*, 2017, **102**, 21–25.
62 N. Iswarya, M. G. Kumar, K. S. Rajan and R. J. B. Balaguru, *Asian J. Sci. Res.*, 2012, **5**, 247–254.
63 N. E. Tari, A. Tadjarodi, J. Tamnanloo and S. Fatemim, *J. CO2 Util.*, 2016, **14**, 126–134.
64 S. Mosleh, M. R. Rahimi, M. Ghaedi, K. Dashtian and S. Hajati, *RSC Adv.*, 2016, **6**, 17204–17214.
65 J. Zhou, X. Li, L. Yang, S. Yan, M. Wang, D. Cheng, Q. Chen, Y. Dong, P. Liu, W. Cai and C. Zhang, *Anal. Chim. Acta*, 2015, **899**, 57–65.
66 Q. Chen, X. Li, X. Min, D. Cheng, J. Zhou, Y. Li, Z. Xie, P. Liu, W. Cai and C. Zhang, *J. Electroanal. Chem.*, 2017, **789**, 114–122.
67 S. Aryanejad, G. Bagherzade and A. Farrokhi, *Inorg. Chem. Commun.*, 2017, **81**, 37–42.
68 S. W. Li, R. M. Gao, R. L. Zhang and J. S. Zhao, *Fuel*, 2016, **184**, 18–27.
69 J. B. Raoof, S. R. Hosseini, R. Ojani and S. Mandegarzad, *Energy*, 2015, **90**, 1075–1081.
70 L. Ai, X. Liu and J. Jiang, *J. Alloys Compd.*, 2015, **625**, 164–170.

71 S. W. Li, J. R. Li, Q. P. Jin, Z. Yang, R. L. Zhang, R. M. Gao and J. S. Zhao, *J. Hazard. Mater.*, 2017, **337**, 208–216.
72 M.-J. Tian, F. Liao, Q.-F. Ke, Y.-J. Guo and Y.-P. Guo, *Chem. - Eur. J.*, 2017, **328**, 962–976.
73 D. Chen, C. Chen, W. Shen, H. Quan, S. Chen, S. Xie, X. Luo and L. Guo, *Adv. Powder Technol.*, 2017, **28**, 1769–1779.
74 J. H. Cui, C. F. Hu, Y. H. Yang, Y. J. Wu, L. F. Yang, Y. L. Wang, Y. L. Liu and Z. Y. Jiang, *J. Mater. Chem.*, 2012, **22**, 8121–8126.
75 X. Xiao, S. Peng, C. Wang, D. Cheng, N. Li, Y. Dong, Q. Li, D. Wei, P. Liu, Z. Xie, D. Qu and X. Li, *J. Electroanal. Chem.*, 2019, **841**, 94–100.
76 T. Aydan, C. Yang, Y. Xu, T. Yuan, M. Zhang, H. Li, X. Liu, X. Su and J. Wang, *Inorg. Chem. Commun.*, 2019, **102**, 162–170.
77 N. E. Tari, A. Tadjarodi, J. Tamnanloo and S. Fatemi, *Microporous Mesoporous Mater.*, 2016, **231**, 154–162.
78 J. Ying, Z.-Y. Hu, X.-Y. Yang, H. Wei, Y.-X. Xiao, C. Janiak, S.-C. Mu, G. Tian, M. Pan, Gu. V. Tendeloob and B.-L. Su, *Chem. Commun.*, 2016, **52**, 8219–8222.
79 L. R. Pizzo, P. G. Vásquez, C. V. Cáceres and C. V. Blanco, Proceedings of the 17th Symposium Iberoam, *Catalysts*, 2000, **1**, 563.
80 L. R. Pizzio, P. G. Vásquez, C. V. Cáceres and M. N. Blanco, *Appl. Catal., A*, 2003, **256**, 125–139.
81 P. Carnitia, A. Gervasinia, F. Bossolab and V. D. Santo, *Appl. Catal., B*, 2016, **193**, 93–102.
82 C. R. Reddy, G. Nagendrappa and B. S. Jai Prakash, *Catal. Commun.*, 2007, **8**, 241–246.
83 M. N. Alaya and M. A. Rabah, *J. Alloys Compd.*, 2013, **575**, 285–291.
84 W. Yu, Y. P. Hsu and C. S. Tan, *Appl. Catal., B*, 2016, **196**, 185–192.
85 Y. Miao, S. Li, L. Gao and G. Xiao, *Mol. Catal.*, 2017, **436**, 128–137.
86 H. Liu, R. Fang, Z. Li and Y. Li, *Chem. Eng. Sci.*, 2015, **122**, 350–359.
87 A. Gupta, D. Kour, V. K. Gupta and K. K. Kapoor, *Tetrahedron Lett.*, 2016, **57**, 4869–4872.
88 H. Taghrir, M. Ghashang and M. N. Biregan, *Chin. Chem. Lett.*, 2016, **27**, 119–126.
89 S. A. R. Mulla, T. A. Salama, M. Y. Pathan, S. M. Inamdar and S. S. Chavan, *Tetrahedron Lett.*, 2013, **54**, 672–675.
90 Z. K-Jaberi and H. Fakhraei, *Bull. Chem. Soc. Ethiop.*, 2012, **26**, 473–478.
91 A. R. Supale and G. S. Gokavi, *J. Chem. Sci.*, 2010, **122**, 189–192.